Semina
Ciências Exatas e Tecnológicas

e-ISSN 1679-0375
ENGINEERING

ORIGINAL ARTICLE DOI 10.5433/1679-0375.2025.v46.52272

# Numerical Study of the Influence of Blood Viscosity on Aortic Blood Flow with Left Ventricular Assistance Support Pump

# Estudo Numérico da Influência da Viscosidade do Sangue no Fluxo Sanguíneo Aórtico com Bomba suporte de Assistência Ventricular Esquerda

Áurelio Ferreira da Costa[1], Alexandre Marconi de Souza da Costa[2]

*Received: January 31, 2025* *Received in revised form: May 6, 2025* *Accepted: June 26, 2025* *Available online: July 8, 2025*

## ABSTRACT

Heart failure (HF) is a condition responsible for thousands of deaths each year. It is characterized by the heart's inability to effectively supply blood to the systemic circulation. In such cases, the implantation of a pump known as a left ventricular assist device (LVAD) helps a failing heart restore proper blood flow. However, LVAD implantation may lead to complications such as an increased risk of stroke, thrombus formation, and reverse flow through the aortic valve. This study aims to numerically investigate a section of the aorta coupled to a LVAD pump, using computational fluid dynamics. The objective is to identify how increased LVAD pump speed and blood viscosity impact hemodynamic variables, which may contribute to the adverse effects of mechanical support. Real data from a patient with an implanted LVAD support were analysed using six viscosity models and five different LVAD pump flow rates. Several simulations were conducted to compare the hemodynamic variables' results across different viscosity models. Subsequently, the results for the various LVAD pump flow rates were analyzed. These analyses allowed the identification of critical points within the geometry, associated with the adverse effects of each hemodynamic variable.

**keywords** numerical study, left ventricular assist device, computational fluid dynamics, viscosity

## RESUMO

A insuficiência cardíaca (IC) é uma doença que leva milhares de pessoas à morte todos os anos. Ela pode ser caracterizada como a incapacidade do coração de suprir sangue satisfatoriamente na circulação sistêmica. Nesta situação, o implante de uma bomba denominada de dispositivo de assistência ventricular esquerda (LVAD), auxilia o coração com IC, a restabelecer o fluxo sanguíneo. Contudo, o implante da bomba pode trazer consequências como aumento do risco de derrames, formação de trombos e escoamento reverso através da válvula aórtica. O objetivo do presente trabalho é investigar numericamente por meio da fluidodinâmica computacional um trecho da artéria aorta acoplado a um suporte de bomba LVAD. Buscando identificar a influência do aumento da velocidade da bomba LVAD e da viscosidade do sangue nas variáveis hemodinâmicas que podem influenciar nos efeitos colaterais do suporte mecânico. Utilizando- se de seis modelos de viscosidade e cinco diferentes vazões da bomba LVAD, foram utilizados dados reais de um paciente implantado com suporte LVAD. Diversas simulações foram realizadas para comparar os resultados das variáveis hemodinâmicas entre diferentes modelos de viscosidade. Em seguida, foram analisados os resultados para as diversas vazões da bomba LVAD. Essas análises permitiram identificar os possíveis pontos críticos na geometria, associados aos efeitos colaterais para cada variável hemodinâmica.

**palavras-chave** estudo numérico, dispositivo de assistência ventricular esquerda, fluidodinâmica computacional, viscosidade

---

[1] MSc., Dpto of Mechanical Engineering, UEM, Maringá, Pr, Brazil. pg404264@uem.br
[2] Prof. Dr., Dpto of Mechanical Engineering, UEM, Maringá, Pr, Brazil. amscosta@uem.br

## Introduction

Heart failure (HF) is a cardiovascular disease responsible for thousands of deaths every year worldwide (Gao et al., 2023; Pandey et al., 2020). This condition is characterized by the inability of the heart to supply arterial blood, rich in oxygen and nutrients, to the body's cells and organs. To support the heart in managing heart failure (HF), mechanical pumps have been developed to assist with pumping blood. Several types of pumps have been developed, which help with the function of the heart: left ventricular assist devices (LVADs), right ventricular assist devices (RVADs), biventricular assist devices (BIVADs), and the total artificial heart (TAH) (Bakouri et al., 2022). Among these, the ones that are most applied clinically are the left ventricular assist devices (LVADs) (Han & Trumble, 2019).

LVAD support has helped thousands of patients with heart failure (HF) achieve a better quality of life by improving systemic circulation throughout the body (Mancini & Colombo, 2015). However, despite these advancements associated with such devices, there are still many challenges to be overcome, related to diseases caused by using LVAD support: ventricular arrhythmias, thrombosis, right heart failure, infections, pump thrombosis, reverse flow in the aortic valve, and bleeding (Bonnemain et al., 2013; Zhang et al., 2016). Approximately 25% of patients develop mild or moderate aortic insufficiency (AI) within the first year of use, and nearly 33% of patients develop moderate or severe AI between the second and third years of LVAD use (Grinstein et al., 2022).

The development of aortic insufficiency (AI) following LVAD implantation is attributed to increased incidence pressures and shear stresses on the aortic valve. These changes cause the valve leaflets to deform and elongate abnormally, resulting in gaps during closure. These gaps allow blood to return, creating retrograde flow through the aortic valve, known as AI. This condition is progressive and tends to worsen over time (Holtz & Teuteberg, 2014; Sun et al., 2020).

As AI progresses, one alternative is to increase the speed of the LVAD pump. This results not only in an increase in net systemic flow, but also increases vessel wall shear stress (WSS) and pressures on the aortic valve, thereby exacerbating AI and reverse flow through the aortic valve (Grinstein et al., 2022).

Advancements in scientific computing and computational fluid dynamics (CFD) have made it possible to solve complex problems in many areas of engineering and medicine through computer simulation. CFD software solves the differential conservation equations for mass and momentum in patient-specific anatomical domains, providing results such as velocity fields, pressure, and stresses (Mannan & HN, 2022).

Several studies have investigated the effect of blood viscosity models on the results of hemodynamic simulations in various regions of the circulatory system: Lee and Steinman (2007) investigated the influence of viscosity models in the carotid artery; Xiang et al. (2012) investigated the effects of viscosity models on carotid artery aneurysms; Caballero and Laín (2015) evaluated the influence of viscosity models on specific aorta arteries, observing their capacity and limitations; Doost et al. (2016) investigated the effects of viscosity models in the left ventricle; Laboni et al. (2019) investigated the influence of viscosity models on coronary arteries; Sun et al. (2020) evaluated the use of mechanical support (CF-LVAD) with constant and variable velocity and applied a non-Newtonian model to evaluate blood characteristics; and Faraji et al. (2023) investigated the influence of viscosity models in an aortic artery with aneurysm.

The aim of this research is to conduct a numerical investigation, through computational fluid dynamics, of a section of the aortic artery coupled to an LVAD pump support, seeking to identify the influence of increasing LVAD pump speed and blood viscosity on hemodynamic variables that may influence the side effects of mechanical support. This is done using six viscosity models: Newtonian and non-Newtonian (Carreau, Casson, Herschel-Bulkley, Power Law, and Carreau-Yasuda).

## Materials and methods

The 3D geometry, used in the simulation process was derived from medical imaging data previously reported by Grinstein et al. (2022), corresponding to a 50-year-old patient implanted with a HeartMate 3 device (HM3, Abbott, Chicago, IL, United States) at the University of Chicago Hospital. The original study received ethics committee approval and informed consent, and the present work used the geometry in accordance with those conditions, without accessing any additional patient data.

In Figure 1(a), we have an illustration of how the LVAD mechanical support works (Song et al., 2022). The geometry consists of the cannula through which the blood pumped by the support of the LVAD passes, and three regions of the aorta artery (ascending aorta, aortic arch, and descending aorta), shown in Figure 1(b). Also in Figure 1(b) is depicted are the two inlets (cannula inlet and aortic root) and five outlets: right subclavian artery (RSA), right common carotid artery (RCCA), left subclavian artery (LSA), left common carotid artery (LCCA), and descending aorta (DA).

**Figure 1 -** Illustrations related to the LVAD system: (a) schematic representation of the mechanical support operation, and (b) corresponding 3D geometry.

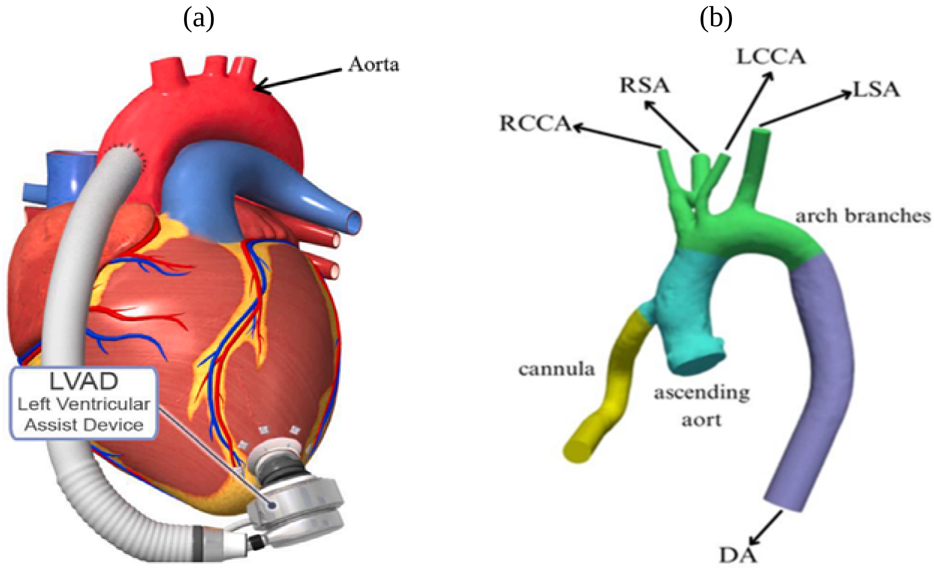

(a) From "Numerical study of hemolysis induced by shear stress at the junction between aorta and ventricular assistance device outflow graft", by J. Song et al., 2022, and (b) From adapted “A computational study of aortic insufficiency in patients supported with continuous flow left ventricular assist devices: Is it time for a paradigm shift in management?”, by J. Grinstein et al., 2022.

The inlet conditions for the pulsatile flow into the aortic root and LVAD support cannula were obtained from a previous study (Grinstein et al., 2022), corresponding to the 0D simulation of the cardiovascular system in a closed circuit. The 0D simulation considers the global circulation of blood in the arteries and veins, the four heart chambers and their valves, the pulmonary circulation, and the LVAD support connected to the left ventricle and the aorta artery (Neidlin et al., 2016).

Thus, based on this 0D solution, it was possible to determine the flow conditions at the root of the aorta and at the entrance of the LVAD cannula. Five studies were conducted with different pulsatile flow rates in L/min at the LVAD cannula inlet and the aortic root, as well as varying regurgitant fraction (RF) rates, which correspond to the backflow occurring when the aortic valve does not function properly.

The five distinct flow rates were designated as Cases (I) to (V), representing the five scenarios of the study. The successive increases in the LVAD rotational speed, and consequently the flow rate, describe the approach used by specialists to treat the worsening of aortic valve insufficiency (AI). In turn, the increase in flow rate may lead to undesirable side effects. These conditions and case designations are summarized in Table 1, where $Q_{\text{LVAD}}$ represents the LVAD support flow rate, and $Q_{\text{ref\_val}}$ denotes the backflow through the aortic valve.

**Table 1 -** Specifications of inlet flow rates and RF for the five LVAD support flow rates.

| **Cases** | **(I)** | **(II)** | **(III)** | **(IV)** | **(V)** |
|---|---|---|---|---|---|
| $Q_{\text{LVAD}}$ [l/min] | 4.61 | 6.08 | 7.31 | 7.92 | 5.01 |
| $Q_{\text{ref\_val}}$ [l/min] | -1.37 | -2.36 | -3.21 | -5.05 | 0.0 |
| RF [%] | 30 | 39 | 44 | 64 | 0.0 |

The Cases (I) to (IV) presented in Table 1 describe the increase in the LVAD support flow rate, but also the intensification of the RF, presenting flows through both inlets of the mechanical support and the normal flow coming from the left ventricle and entering the beginning of the aortic artery. Case (V) is a particular case, in which all the blood flow is exclusively pumped by the LVAD support. In this scenario, there is no flow through the aortic valve, nor is there any blood reflux. The aortic valve remains completely closed throughout the entire cardiac cycle, reflecting the total dependence of the systemic circulation on the LVAD mechanical support.

At the five outlets, 3-element Windkessel (RCZ) boundary conditions were specified. In this lumped parameter model, based on a hydraulic-electrical analogy, R represents proximal resistance, C represents capacitance, and Z represents distal resistance or a characteristic impedance of the arterial network (Brown et al., 2012; Li & Mao, 2023; Shi et al., 2011). A compiled user-defined function (UDF) in C language was coupled to the ANSYS Fluent solver to specify the Windkessel boundary conditions at the outlets. The values used are presented in Table 2.

**Table 2 -** Values of the Windkessel model.

| **Outlets** | **R** (kg $m^{-4}$ $s^{-1}$) | **C** ($kg^{-1}$ $m^4$ $s^2$) | **Z** (kg $m^{-4}$ $s^{-1}$) |
|---|---|---|---|
| RSA | $1.8\times10^9$ | $10^{-11}$ | $1.8\times10^9$ |
| RCCA | $1.29\times10^9$ | $10^{-11}$ | $1.29\times10^9$ |
| LSA | $1.8\times10^9$ | $10^{-11}$ | $1.8\times10^9$ |
| LCCA | $1.29\times10^9$ | $10^{-11}$ | $1.29\times10^9$ |
| DA | $1.18\times10^9$ | $10^{-11}$ | $1.18\times10^9$ |

The CFD simulations were conducted using the ANSYS Fluent solver (ANSYS ACADEMIC RESEARCH 16.0). The hardware used was a laptop with a 12th Gen Intel(R) Core(TM) i7-12700H 2.30 GHz processor, 16.0 GB of RAM, a 64-bit operating system, Windows 11 edition, version 23H2. Each simulation required approximately 74 hours. The mesh was composed using the Fluent meshing tool, with a total of 733,299 polyhedric hexa-core cells. The mesh and details of the solver settings can be found in the Supplementary Material and Data Section.

## *Set of simulations*

In the first set of simulations, which is considered the reference case Newtonian, the following conditions were adopted:

- Incompressible and Newtonian fluid, viscosity 0.0035 kg/(m·s), density 1060 kg/$m^3$;
- Rigid vessel wall;
- Laminar flow;
- Boundary conditions at inlets: volumetric flow rate in [$m^3$/s];
- Outlet boundary conditions: 3-element Windkessel model (RCZ).

The above conditions must also be interpreted as limitations of the current study.

In the second set of simulations, the Carreau viscosity model was employed. This viscosity model is described in equation (1), by

$$\mu = \eta_\infty + (\eta_0 - \eta_\infty)\left[1 + k^2\gamma^2\right]^{\frac{n-1}{2}}, \tag{1}$$

where $\mu$ is the viscosity in kg/(m·s), $k$ is a time constant (s), $n$ is the power law index, and $\eta_0$ and $\eta_\infty$ are the upper and lower limits of viscosity corresponding to low and high shear stress, with units in kg/(m·s) (Pandey et al., 2020).

In the third set of simulations, where we employed the Casson viscosity model, all conditions from the first simulation were maintained, except for the viscosity model, which was described by equation (2):

$$\mu = \frac{\tau_0}{\gamma} + \sqrt{\frac{\eta\tau_0}{\gamma}} + \eta, \tag{2}$$

where $\mu$ is the viscosity, in kg/(m·s), $\gamma$ is the strain rate in s$^{-1}$, $\tau_0$ is the yield stress in Pa, and $\eta$ is the Casson rheological constant (Pandey et al., 2020).

In the fourth set of simulations, the viscosity used was given by the Herschel-Bulkley model, according to equation (3):

$$\mu = K\dot{\gamma}^{n-1} + \frac{\tau_0}{\dot{\gamma}}, \tag{3}$$

where $\mu$ is the viscosity, in kg/(m·s), $\tau_0$ is the yield stress, in Pa, $\dot{\gamma}$ is the shear rate in s$^{-1}$, $n$ is the dimensionless power-law index from 0 to 1, and $K$ is the consistency index in kg·s$^{n-2}$/m (Faraji et al., 2023).

The fifth viscosity model was given by the Carreau–Yasuda model, as expressed in equation (4):

$$\mu(\dot{\gamma}) = \mu_\infty + \frac{\mu_0 - \mu_\infty}{[1 + (\lambda\dot{\gamma})^2]^{1/3}}, \tag{4}$$

where $\mu$ is the viscosity [kg/(m·s)], $\mu_\infty$ is the viscosity for the infinite shear rate [kg/(m·s)], $\mu_0$ is the viscosity for the zero shear rate [kg/(m·s)], and $\lambda$ is the relaxation time in s (Prather et al., 2021).

The sixth viscosity model was given by the power law model, expressed by

$$\mu = \mu_0\dot{\gamma}^{n-1}. \tag{5}$$

In equation (5) $\mu$ is the viscosity in kg/(m·s), $\mu_0$ is the viscosity at zero shear rate in kg/(m·s), $\dot{\gamma}$ is the deformation rate in s$^{-1}$, and $n$ is the dimensionless power law index (Jahangiri et al., 2017).

The behavior of different viscosity models as a function of shear rate for blood flow was evaluated by Faraji et al. (2023) and Jahangiri et al. (2017), as illustrated in Figure 2.

**Figure 2 -** Predictions of blood viscosity as a function of shear rate for the viscosity models by: (a) Faraji et al. (2023), and (b) Jahangiri et al. (2017).

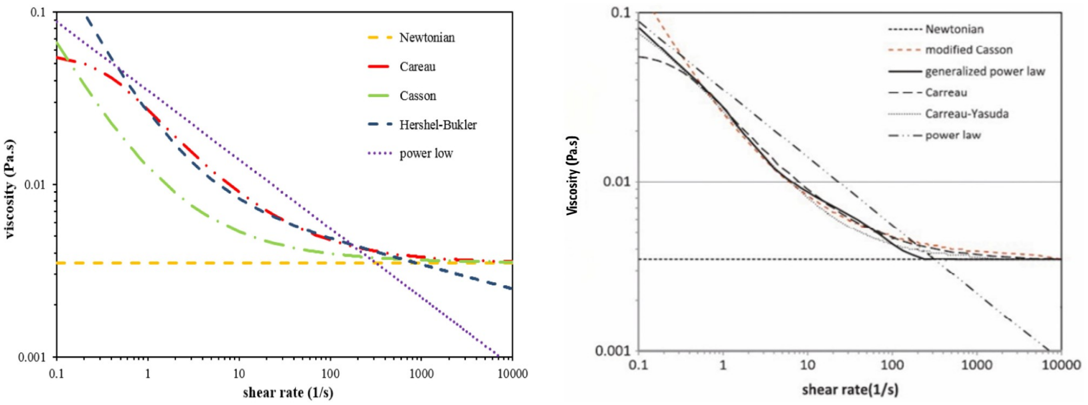

(a) (b)

Figures 2(a) and 2(b) show the predicted blood viscosity as a function of the shear rate for different viscosity models. It can be observed that, at low shear rates, all non-Newtonian models exhibit higher viscosity compared to the Newtonian model. However, as the shear rate increases, these differences gradually decrease.

In the shear rate range between 100 and 1000 (1/s), the models converge to a similar blood viscosity value, around 0.003 to 0.004 Pa·s. In the shear rate range from 1000 to 10,000 (1/s), as illustrated in Figure 2(a), two models stand out by deviating from the others: the power-law model and the Herschel-Bulkley model.

The power-law model exhibits a characteristic linear decrease in viscosity with increasing shear rate, a phenomenon also evident in Figure 2(b). In contrast, the Herschel-Bulkley model displays a sinusoidal pattern of decreasing viscosity as the shear rate increases.

On the other hand, the Carreau, Carreau-Yasuda, Casson, modified Casson, and modified power-law models tend to converge to a common viscosity value when subjected to high shear rates.

## Results and discussion

In the analysis of different flow cases and viscosity models at the moment of peak flow of the LVAD support for the velocity field variable, it was observed that, as the variable increased, the regions of maximum velocity occurred in the same areas. This trend is illustrated in Figure 3.

**Figure 3 -** Comparative velocity vector for the five flow rates ($Q$) support LVAD: (a) $Q = 4.61$, (b) $Q = 6.08$, (c) $Q = 7.31$, (d) $Q = 7.92$, (e) $Q = 5.01$ [l/min], and (f) Velocity magnitude colormap ranging.

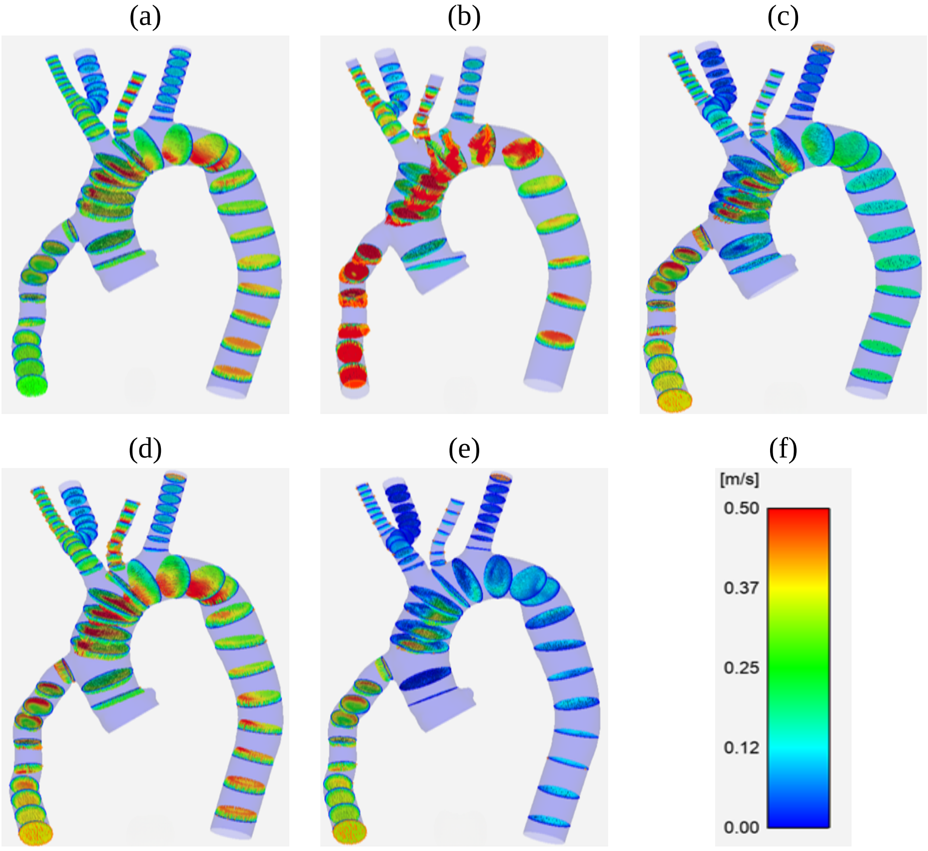

We can observe that the lowest velocities occurred in Case (V), illustrated in Figure 3(e), where the highest velocities are mainly located in the cannula and the ascending aorta. Next, there is Case (III), illustrated in Figure 3(c), in which the regions of maximum velocity remain the same, located in the cannula and the ascending aorta. The increase in maximum velocity becomes particularly evident in the ascending aorta. This trend of increasing maximum velocity is observed sequentially in Case (I), illustrated in Figure 3(a), followed by Case (IV) in Figure 3(d), and finally in Case (II), illustrated in Figure 3(b). In this case, the regions of maximum velocity are the highest among all analyzed, occurring in the cannula, the ascending aorta, the descending aorta, and the smaller-diameter arteries, including the right and left common carotid arteries.

### *Wall shear stress (WSS) analysis*

The wall shear stress (WSS), an important hemodynamic indicator, reveals areas prone to thrombus and aneurysm formation, which may result in a potential rupture of the vessel wall (Xiang et al., 2012).

Table 3 illustrates the WSS values for the five flow rates of the LVAD support. A significant variation in these values is observed, with Case (II) recording the highest values of this variable. Compared to Case (V), which recorded the lowest value, Case (II) exhibited an increase of approximately 192%, representing more than a doubling of the value observed in Case (V), and indicating a substantial elevation. Cases (I) and (IV) exhibited very similar values, with a percentage variation of less than 7% between them.

**Table 3 -** Maximum WSS values for each LVAD flow rate averaged across the six viscosity models.

| **Cases** | **Support flow LVAD** | | | | |
|---|---|---|---|---|---|
| | **(I)** | **(II)** | **(III)** | **(IV)** | **(V)** |
| $Q$ (l/min) | 4.61 | 6.08 | 7.31 | 7.92 | 5.01 |
| WSS$_{max}$ [Pa] | 11.10 | 23.88 | 9.27 | 11.84 | 8.17 |

The distribution of WSS is shown in Figure 4, where it can be observed that the maximum values occur in the same regions as the variable increases. In Case (V), illustrated in Figure 4(e), the lowest WSS value is recorded among all the cases studied, with the maximum concentrated in the region where the cannula connects to the ascending aorta.

**Figure 4 -** Wall Shear Stress (WSS) for the five flow rates ($Q$) support LVAD: (a) $Q = 4.61$, (b) $Q = 6.08$, (c) $Q = 7.31$, (d) $Q = 7.92$, (e) $Q = 5.01$ [l/min], and (f) Shear stress magnitude colormap ranging.

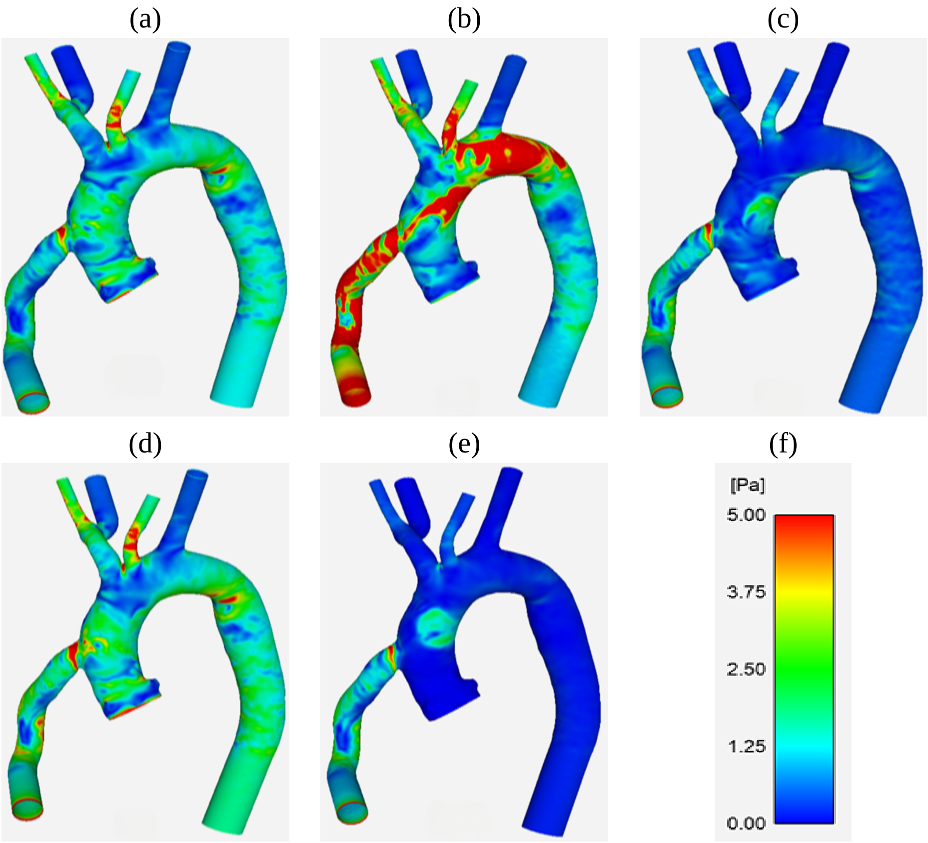

According to Table 3, Case (III), illustrated in Figure 4(c), presents the second lowest WSS value, with the maximum occurring in the same region as in Case (V), that is, in the area where the cannula connects to the ascending aorta, but with a slightly higher intensity. Upon closer observation, it can be noted that some regions of the geometry begin to stand out through a change in color, especially in the smaller-diameter arteries, such as the left and right carotids, as well as in the region of the aorta at the end of the aortic arch and at the beginning of the descending aorta. In these areas, regions of maximum values begin to appear, which become even more pronounced in Case (I), which shows a slightly higher WSS value compared to Case (III).

In sequence, Case (I) presents the third lowest value among the analyzed cases. The same maximum regions observed in the first two cases remain present, including the area where the cannula connects to the ascending aorta. Additionally, the regions of the smaller-diameter arteries, such as the left and right carotids, as well as the region of the aorta at the end of the aortic arch and the beginning of the descending aorta—where the artery forms a curve—become more evident. In Case (III), these regions were already slightly highlighted, but now they consolidate as areas of maximum WSS, represented by the red color. The same occurs in Case (IV), but with a slightly higher intensity of the variable.

Finally, in Case (II), which presented the highest WSS value, 23.88 Pa, the same peak regions identified in the previous cases are observed, but with greater intensity. Additionally, new regions of interest emerge, including areas within the cannula and the region of the aortic arch.

## *Time-averaged wall shear stress (TAWSS)*

The temporal average of wall shear stress (TAWSS) is used to measure the average WSS throughout the entire cardiac cycle. Table 4 illustrates the TAWSS values for the five flow rates of the LVAD support.

**Table 4 -** Maximum TAWSS values for each LVAD support flow rate averaged across the five viscosity models.

| **Cases** | **Support flow LVAD** | | | | |
|---|---|---|---|---|---|
| | **(I)** | **(II)** | **(III)** | **(IV)** | **(V)** |
| $Q$ (l/min) | 4.61 | 6.08 | 7.31 | 7.92 | 5.01 |
| TAWSS$_{max}$ [Pa] | 4.43 | 15.23 | 7.37 | 8.31 | 4.86 |

According to Table 4, Case (II) presented the highest TAWSS values, with an increase of approximately 244% and 213% compared to Cases (I) and (V), respectively, corresponding to values nearly three times greater than those observed in these cases, indicating that TAWSS followed the same trend observed for WSS. Furthermore, as with WSS, the maximum TAWSS values occur sequentially in the same regions as the variable increases, as illustrated in Figures 5(a) to 5(e).

**Figure 5 -** Temporal average of wall shear stress (TAWSS) comparative for the five flow rates ($Q$) support LVAD: (a) $Q = 4.61$, (b) $Q = 6.08$, (c) $Q = 7.31$, (d) $Q = 7.92$, (e) $Q = 5.01$ [l/min], and (f) Shear stress magnitude colormap ranging.

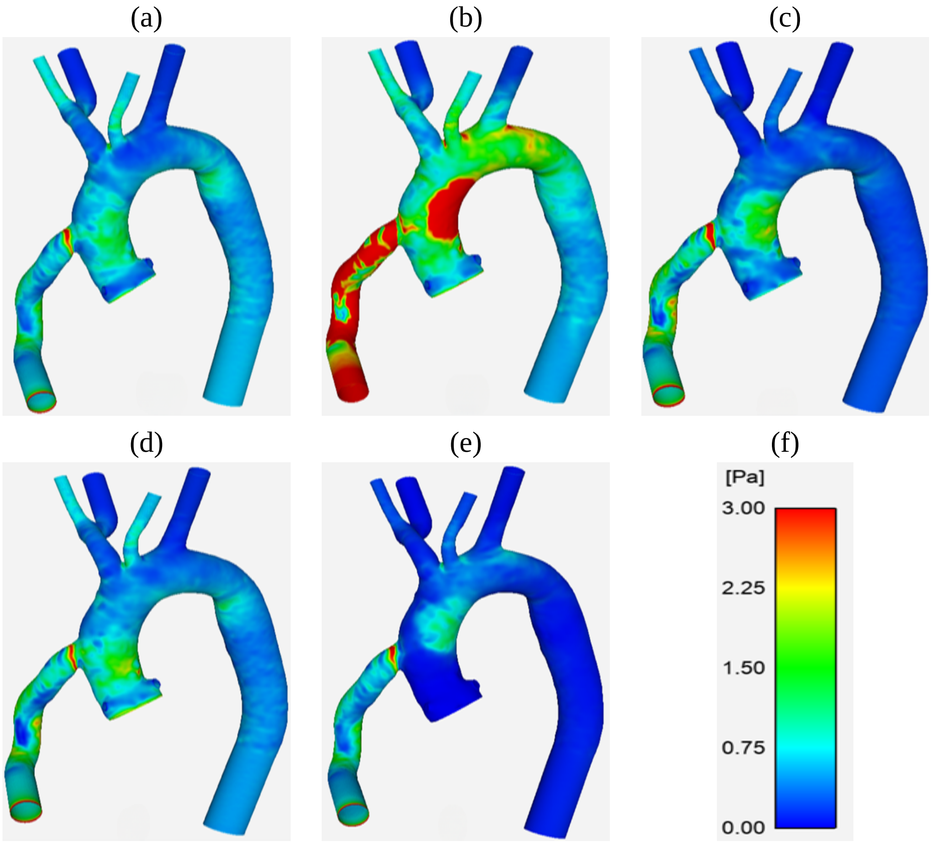

Case (I) showed the lowest TAWSS value, with the maximum values located in the region where the cannula connects to the ascending aorta. It is observed that some regions of the geometry begin to stand out due to a change in color, especially in the aorta, opposite from the flow entry from the cannula.

Sequentially, the maximum regions increase as the TAWSS value rises in Cases (V), (III), and (IV), until reaching Case (II), which records the highest TAWSS value of 15.23 Pa. In this last case, the same maximum regions observed previously are identified, but with greater intensity. Additionally, new areas of interest emerge, including parts of the cannula and the region of the aortic arch.

### *Strain rate distribution*

Table 5 presents the wall deformation rate values for the five study cases, once again highlighting that Case (II) displays the highest values of this variable. Additionally, as observed for other hemodynamic variables, the maximum values occur in the same regions as the variable increases. This behavior is clearly illustrated in Figure 6.

**Table 5 -** Maximum deformation rate values for each LVAD support flow rate averaged across the five viscosity models.

| **Cases** | **Support flow LVAD** | | | | |
|---|---|---|---|---|---|
| | **(I)** | **(II)** | **(III)** | **(IV)** | **(V)** |
| $Q$ (l/min) | 4.61 | 6.08 | 7.31 | 7.92 | 5.01 |
| Defor$_{max}$ [1/s] | 3557.00 | 6384.00 | 2306.00 | 3553.00 | 1742.00 |

**Figure 6 -** Comparative deformation rate for the 5 LVAD support flow rates ($Q$) support LVAD: (a) $Q = 4.61$, (b) $Q = 6.08$, (c) $Q = 7.31$, (d) $Q = 7.92$, (e) $Q = 5.01$ [l/min], and (f) Strain rate magnitude colormap ranging.

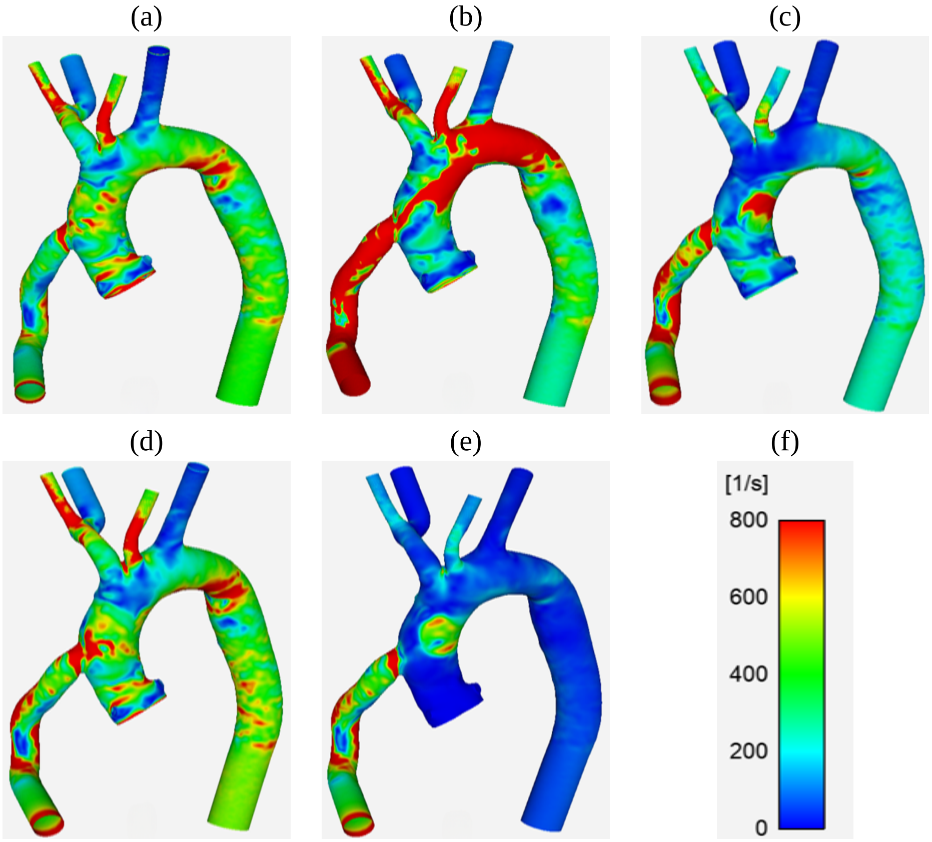

Case (V), shown in Figure 6(e), presents the lowest deformation rate. In this scenario, peak regions are located in the cannula and in the wall of the ascending aorta opposite the flow entry from the cannula, and, with lower intensity, in the smaller-diameter arteries, such as the left and right carotid arteries. Additional peaks are also observed in the aorta at the end of the aortic arch and at the beginning of the descending aorta, where the artery forms a curvature.

These same maximum regions are repeated in Cases (III), (IV), and (V), with increasing values and a larger affected area. In Case (II), which presents the highest deformation rate value of 6384.00 (1/s), as illustrated in Figure 6(b), the maximum regions observed in the previous cases appear with even greater intensity and extent. Moreover, new regions are affected, particularly in the area of the aortic arch near the origin of the left subclavian artery.

## Conclusions

Based on the viscosity models employed and the different flow rates of LVAD support, regions of the geometry were identified as critical points for potential side effects associated with mechanical LVAD assistance. These analyses were carried out for each hemodynamic variable, as detailed below:

Velocity Fields: The study showed that, with the intensification of velocity vector fields across different flow rates and viscosity models, certain regions stand out as critical. Notably, the aortic arch and the two smaller-diameter arteries—the right common carotid artery (RCCA) and the left common carotid artery (LCCA)—presented the highest velocity values, indicating areas of particular hemodynamic stress.

Hemodynamic Variable WSS: The critical regions for wall shear stress (WSS) include:

- The coupling region of the cannula in the aortic artery;
- The region opposite to the inflow from the cannula in the aortic artery;
- The aortic arch;
- The right and left common carotid arteries (RCCA and LCCA);
- The end of the aortic arch and the beginning of the descending aorta, where a change in flow direction occurs due to the arterial curvature.

Hemodynamic Variable TAWSS: The critical regions for time-averaged wall shear stress (TAWSS) include:

- The coupling region of the cannula in the aortic artery;
- The ascending aorta;
- The region opposite to the inflow from the cannula;
- The aortic arch.

Hemodynamic Variable: Deformation Rate: Regions exhibiting high strain rate values were identified as potential sites for side effects associated with mechanical circulatory support, such as an increased risk of thrombogenesis (Casa et al., 2015). The critical regions include:

- The ascending aorta;
- The aortic arch;
- The RCCA and LCCA;
- The end of the aortic arch and the beginning of the descending aorta, where the curvature contributes to increased deformation rates.

In conclusion, the robustness and applicability of the present results should be further assessed through additional simulations, considering, for instance, physiological data from various implanted patients, multiphase flow dynamics, and deformable vessel walls.

### *Author contributions*

**A. F. da Costa** contributed to: data curation, formal analysis, investigation, resources, visualization, writing – original draft, writing. **A. M. de S. da Costa** contributed to: conceptualization, methodology, project administration, software, supervision, validation, writing – review & editing.

### *Conflicts of interest*

The authors declare no conflict of interest.

## *Supplementary material and data*

Available at: https://doi.org/10.5281/zenodo.15012298

## *Acknowledgements*

Our thanks to researcher Professor Dr. Pablo Javier Blanco, in collaboration with the National Laboratory for Scientific Computing (LNCC), for his numerous relevant contributions to our research.

# References

Bakouri, M., Alassaf, A., Alshareef, K., Smida, A., AlMohimeed, I., Alqahtani, A., Aboamer, M. A., & Alharbi, Y. (2022). A feasible method to control left ventricular assist devices for heart failure patients: A numerical study. *Mathematics*, *10*(13), 2251. https://doi.org/10.3390/math10132251

Bonnemain, J., Malossi, A. C. I., Lesinigo, M., Deparis, S., Quarteroni, A., & von Segesser, L. K. (2013). Numerical simulation of left ventricular assist device implantations: Comparing the ascending and the descending aorta cannulations. *Medical Engineering & Physics*, *35*(10), 1465–1475. https://doi.org/10.1016/j.medengphy.2013.03.022

Brown, A. G., Shi, Y., Marzo, A., Staicu, C., Valverde, I., Beerbaum, P., Lawford, P. V., & Hose, D. R. (2012). Accuracy vs. computational time: Translating aortic simulations to the clinic. *Journal of Biomechanics*, *45*(3), 516–523. https://doi.org/10.1016/j.jbiomech.2011.11.041

Caballero, A. D., & Laín, S. (2015). Numerical simulation of non-newtonian blood flow dynamics in human thoracic aorta. *Computer Methods in Biomechanics and Biomedical Engineering*, *18*(11), 1200–1216. https://doi.org/10.1080/10255842.2014.887698

Casa, L. D., Deaton, D. H., & Ku, D. N. (2015). Role of high shear rate in thrombosis. *Journal of vascular surgery*, *61*(4), 1068–1080. https://doi.org/10.1016/j.jvs.2014.12.050

Doost, S. N., Zhong, L., Su, B., & Morsi, Y. S. (2016). The numerical analysis of non-newtonian blood flow in human patient-specific left ventricle. *Computer Methods and Programs in Biomedicine*, *127*, 232–247. https://doi.org/10.1016/j.cmpb.2015.12.020

Faraji, A., Sahebi, M., & SalavatiDezfouli, S. (2023). Numerical investigation of different viscosity models on pulsatile blood flow of thoracic aortic aneurysm (taa) in a patient-specific model. *Computer Methods in Biomechanics and Biomedical Engineering*, *26*(8), 986–998. https://doi.org/10.1080/10255842.2022.2102423

Gao, X., Xu, Z., Chen, C., Hao, P., He, F., & Zhang, X. (2023). Full-scale numerical simulation of hemodynamics based on left ventricular assist device. *Frontiers in Physiology*, *14*, 1192610. https://doi.org/10.3389/fphys.2023.1192610

Grinstein, J., Blanco, P. J., Bulant, C. A., Torii, R., Bourantas, C. V., Lemos, P. A., & Garcia-Garcia, H. M. (2022). A computational study of aortic insufficiency in patients supported with continuous flow left ventricular assist devices: Is it time for a paradigm shift in management? *Frontiers in Cardiovascular Medicine*, *9*, 933321. https://doi.org/10.3389/fcvm.2022.933321

Han, J., & Trumble, D. R. (2019). Cardiac assist devices: Early concepts, current technologies, and future innovations. *Bioengineering*, *6*(1), 18. https://doi.org/10.3390/bioengineering6010018

Holtz, J., & Teuteberg, J. (2014). Management of aortic insufficiency in the continuous flow left ventricular assist device population. *Current heart failure reports*, *11*, 103–110.

Jahangiri, M., Saghafian, M., & Sadeghi, M. R. (2017). Numerical simulation of non-newtonian models effect on hemodynamic factors of pulsatile blood flow in elastic stenosed artery. *Journal of Mechanical Science and Technology*, *31*, 1003–1013. https://doi.org/10.1007/s12206-017-0153-x

Laboni, F. S., Rabbi, M. F., & Arafat, M. T. (2019). Computational analysis of left coronary bifurcating artery using different blood rheological models. AIP Conference Proceedings, *2121*(1), 100002. https://doi.org/10.1063/1.5115933

Lee, S. W., & Steinman, D. A. (2007). On the relative importance of rheology for image-based cfd models of the carotid bifurcation. *Journal of Biomechanical Engineering*, *129*(2), 273–278. https://doi.org/10.1115/1.2540836

Li, Z., & Mao, W. (2023). A fast approach to estimating windkessel model parameters for patient-specific multi-scale cfd simulations of aortic flow. *Computers & Fluids*, *259*, 105894. https://doi.org/10.1016/j.compfluid.2023.105894

Mancini, D., & Colombo, P. C. (2015). Left ventricular assist devices: A rapidly evolving alternative to transplant. *Journal of the American College of Cardiology*, *65*(23), 2542–2555.

Mannan, M. A., & HN, M. F. (2022). Computational fluid dynamics in coronary and intra-cardiac flow simulation. *International Journal for Research in Applied Science & Engineering Technology (IJRASET)*, *10*(7), 688–693. https://doi.org/10.22214/IJRASET.2022.45280

Neidlin, M., Corsini, C., Sonntag, S. J., Schulte-Eistrup, S., Schmitz-Rode, T., Steinseifer, U., Pennati, G., & Kaufmann, T. A. (2016). Hemodynamic analysis of outflow grafting positions of a ventricular assist device using closed-loop multiscale cfd simulations: Preliminary results. *Journal of Biomechanics*, *49*(13), 2718–2725. https://doi.org/10.1016/j.jbiomech.2016.06.003

Pandey, R., Kumar, M., Majdoubi, J., Rahimi-Gorji, M., & Srivastav, V. K. (2020). A review study on blood in human coronary artery: Numerical approach. *Computer Methods and Programs in Biomedicine*, *187*, 105243. https://doi.org/10.1016/j.cmpb.2019.105243

Prather, R., Divo, E., Kassab, A., & DeCampli, W. (2021). Computational fluid dynamics study of cerebral thromboembolism risk in ventricular assist device patients: Effects of pulsatility and thrombus origin. *Journal of Biomechanical Engineering*, *143*(9), 091001. https://doi.org/10.1115/1.4050819

Shi, Y., Lawford, P., & Hose, R. (2011). Review of zero-d and 1-d models of blood flow in the cardiovascular system. *Biomedical Engineering Online*, *10*, 1–38.

Song, J., Marcel, L., Specklin, M., Lescroart, M., Hébert, J. L., & Kouidri, S. (2022). Numerical study of hemolysis induced by shear stress at the junction between aorta and ventricular assistance device outflow graft. *International Journal of Heat and Fluid Flow*, *95*, 108953. https://doi.org/10.1016/j.ijheatfluidflow.2022.108953

Sun, P., Bozkurt, S., & Sorguven, E. (2020). Computational analyses of aortic blood flow under varying speed cf-lvad support. *Computers in Biology and Medicine*, *127*, 104058. https://doi.org/10.1016/j.compbiomed.2020.104058

Xiang, J., Tremmel, M., Kolega, J., Levy, E. I., Natarajan, S. K., & Meng, H. (2012). Newtonian viscosity model could overestimate wall shear stress in intracranial aneurysm domes and underestimate rupture risk. *Journal of Neurointerventional Surgery*, *4*(5), 351–358. https://doi.org/10.1136/neurintsurg-2011-010089

Zhang, Y., Gao, B., & Yu, C. (2016). The hemodynamic effects of the lvad outflow cannula location on the thrombi distribution in the aorta: A primary numerical study. *Computer Methods and Programs in Biomedicine*, *133*, 217–227. https://doi.org/10.1016/j.cmpb.2016.05.017